Effects of the α-cluster structure and the intrinsic momentum component of nuclei on the longitudinal asymmetry in relativistic heavy-ion collisions

Ru-Xin Cao (曹汝鑫) [1,2,3] Song Zhang (张松) [2,4,*] and Yu-Gang Ma (马余刚) [2,4,†]

[1]*Shanghai Institute of Applied Physics, Chinese Academy of Sciences, Shanghai 201800, China*

[2]*Key Laboratory of Nuclear Physics and Ion-beam Application (MOE), Institute of Modern Physics, Fudan University, Shanghai 200433, China*

[3]*School of Nuclear Sciences and Technology, University of Chinese Academy of Sciences, Beijing 100049, China*

[4]*Shanghai Research Center for Theoretical Nuclear Physics, NSFC and Fudan University, Shanghai 200438, China*

The longitudinal asymmetry in relativistic heavy ion collisions arises from the fluctuation in the number of nucleons involved. This asymmetry causes a rapidity shift in the center of mass of the participating zone. Both the rapidity shift and the longitudinal asymmetry have been found to be significant at the top CERN Large Hadron Collider (LHC) energy for collisions of identical nuclei, and the longitudinal asymmetry is important for reconstructing the colliding vertex and correcting the rapidity shift. However, much discussion of the longitudinal asymmetry has treated the initial condition as a nonzero momentum contributed only by the number of participants, i.e., the asymmetry depends only on the number of participating nucleons. So we naturally raise a physical problem, can other initial conditions, such as two typical initial conditions for nuclei, geometric configuration, and momentum distribution, provide effects on the longitudinal asymmetry? Therefore, in this work we consider other effects on the longitudinal asymmetry other than the fluctuation in the number of participants, e.g., the α clustering structure as well as the intrinsic momentum distribution in the target and projectile nuclei for the collisions in the framework of a multiphase transport (AMPT) model. By introducing systems with different α-clustering structure and intrinsic momentum distribution, we calculated the ratio of the rapidity distributions of different systems and extracted expansion coefficients to analyze the difference contributed by these factors. We also investigated the possible effect of the non-Gaussian distribution on the rapidity distribution. These results can help us to constrain the initial conditions and reconstruct the colliding vertex in ultrarelativistic heavy ion collisions, and suggest a quantitative correction on the final state measurement and a possible correlation between the initial condition and the final state observable in LHC and BNL Relativistic Heavy Ion Collider energy.

I. INTRODUCTION

For decades, the relativistic heavy-ion collision experiment has been an important approach to study properties of strong interaction as well as quark-gluon plasma (QGP) which was supposedly existed in the early universe [1–14]. Generally in relativistic heavy-ion collisions, we treat colliding nucleons as two parts, i.e., participants that take part in collisions and spectators that simply pass through the collision zone without interaction. For a collision between nonidentical nuclei, the number of participating nucleons from each nucleus is naturally different. However, for a collision between identical

nuclei, the number of participants may also fluctuate event by event. That means the numbers of participants in two colliding nuclei may also lead to an inequality. This inequality from participant number fluctuation will lead to a nonzero net momentum of the nucleon-nucleon center of mass frame, but assumed fixed momentum for each nucleon in advance. Thus the center of mass of participants will shift from the collider center of mass of the system, further results in the rapidity shift at final state. This effect was usually called longitudinal asymmetry [15,16]. The longitudinal asymmetry reflects the fluctuation of the nucleon at initial state, and may manifest in some phenomena. For instance, the Λ polarization was investigated in Ref. [17] which applied the ultrarelativistic quantum molecular dynamics (UrQMD) model [18–21] and gave global spin polarization of Λ hyperon for ^{108}Ag + ^{108}Ag and ^{197}Au + ^{197}Au collisions at $\sqrt{s_{NN}} = 2.42$–62.4 GeV. In that work it was compared with measurements from the HADES Collaboration [22] and STAR Collaboration [23] and fitted well at lower energies. They concluded that the global polarization was a result of the global angular momentum of the system, so that the longitudinal asymmetry involving

*song_zhang@fudan.edu.cn

†mayugang@fudan.edu.cn

initial momentum spatial asymmetry may also be correlated to the polarization phenomena.

Previous study on longitudinal asymmetry usually focuses on the effects from participant fluctuation between target and projectile. Thus a motivation naturally arises, can other effects at initial state of collision provide additional significant contribution to longitudinal asymmetry? Based on this motivation, we consider two important effects at initial state—α-clustering structure in light nuclei and short range correlation, which may intensify the longitudinal asymmetry.

An α-clustered nucleus was proposed by Gamow [24], which could be regarded as a special case of nuclear structure. In that view, in stable nuclei especially for $4N$ nuclei, some small groups (like α) made up of two protons and two neutrons are likely to exist. Then in the nucleus these groups are connected in different shapes like triangle in ^{12}C, tetrahedron in ^{16}O, and so on. The clustering effect is important to nuclear equation of state, nucleosynthesis, and many other problems [25–28]. Various observables have therefore been proposed to study the clustering of nuclei in the heavy-ion reaction, such as collective flow [29–31] and multiplicity correlation [32,33]. A recent review can be found in [34,35]. So we assume that such geometry configurations are likely to affect the fluctuation of numbers of participants at initial state, and further contribute to the longitudinal asymmetry.

Another effect taken into our account is the short range correlation (SRC). The SRC can partly arise from the nucleon-nucleon short-range central interaction [36,37]. And the intrinsic momentum distribution of nucleons is a direct reflection, which shows us the probability to find a nucleon at certain momentum in a nucleus. When using high values of nucleon momentum and removal energy to describe nucleon spectral function, the function can be written in the form of a convolution integral involving the momentum distributions describing the relative and center-of-mass motion of a correlated nucleon-nucleon pair embedded in the medium [37]. High momentum tail (HMT), as a direct result from SRC, can be found in the momentum distribution of nucleons, and some studies show that the contribution of HMT is mainly provided by proton-neutron pairs [37,38]. In Ref. [39] the related phenomenon in an extended quantum molecular dynamics (EQMD) model has been discussed, and the effects on emission time distribution, momentum spectrum, and momentum correlation function of two emitted protons of the $^{12}C - ^{11}B$ reaction are also investigated, which demonstrate the importance of the SRC. The intrinsic momentum distribution of the nucleon may also affect the shift of initial center of mass, then affect the longitudinal asymmetry.

Under a multiphase transport (AMPT) frame, it is simulated that $^{12}C + ^{12}C$ collisions with/without an α cluster at center of mass energy $\sqrt{s_{NN}} =$ 6.37 TeV and 200 GeV, $^{12}C + ^{12}C$ collisions with/without intrinsic momentum distribution at 200 GeV, as well as $^{197}Au + ^{197}Au$ collisions with Woods-Saxon configuration and high-momentum-tail configuration at 200 GeV. The 0–10 % centrality is always adopted in all simulations. With the same $\sqrt{s_{NN}}$ and configuration (such as the default Woods-Saxon), a comparison between different systems, for example, C + C and Au + Au, reveals the system size dependence of longitudinal asymmetry. Also

for the same configuration like Woods-Saxon, comparison between at 200 GeV and 6.37 TeV in C + C collisions shows us the energy dependence of longitudinal asymmetry. Similarly, at the same $\sqrt{s_{NN}}$, a comparison between systems with Woods-Saxon (WS) and α-cluster reveals the effect on longitudinal asymmetry from geometry configuration, comparison between systems with free-Fermi gas and high-momentum tail reveals an effect on longitudinal asymmetry from intrinsic momentum distribution, in which the high-momentum-tail case can show us how the short range correlation in a nucleon pair changes longitudinal asymmetry.

The paper is organized as follows. In Sec. II, we give brief introductions of the models used in our simulation—the AMPT model, the α cluster structure, and the HMT effect. Then we introduce basic methods to calculate these longitudinal asymmetry parameters and to provide a correction of our α-cluster effect and HMT effect. We also suggested possible reasons to explain the differences between different results, and linked these reasons to some further investigations in later works. In Sec. III, we use AMPT to simulate C + C and Au + Au collisions with different initial conditions, and extract their longitudinal asymmetry parameters and expansion coefficients. We then compare the parameters and coefficients from different systems and point out their differences. In Sec. IV, we explain the effect on longitudinal asymmetry from the initial condition, which can give us insights and guidance on how to constrain the collision conditions, reconstruct the colliding vertex, and relate the observed final state to the effect of different systems in future experimental measurements. Finally, in Sec. V we give the conclusion and outlook of our work.

II. MODELS AND METHODS

A. Introduction to AMPT

A multiphase transport model [40–42] is composed of four stages to simulate relativistic heavy-ion collisions. It has successfully described various phenomena at the BNL Relativistic Heavy Ion Collider (RHIC) and CERN Large Hadron Collider (LHC) energies and becomes a well-known event generator. The AMPT has two versions: string melting (SM) and default. In the SM version, the Heavy Ion Jet Interaction Generator (HIJING) [43,44] is used to simulate the initial conditions, then Zhang's parton cascade (ZPC) [45] is used to describe interactions for partons which are from all hadrons in the HIJING but spectators, after which a simple quark coalescence model describes hadronization process, finally a relativistic transport (ART) model [46] simulates the hadron rescattering process. The default version of AMPT only conducts the minijet partons in partonic scatterings via ZPC and uses the Lund string fragmentation to perform hadronization.

AMPT model [40,42] can describe the p_T spectrum and energy dependence of identified particles such as pion, kaon, ϕ, proton, and Ω produced in heavy-ion collisions [41,47,48], as well as the collective flows and temperature during evolution, etc. [49–53]. Chiral and magnetic related anomalous phenomena can also be described by the AMPT model [54–59]. Further details of the model description and the selection of the parameter set can be found in Refs. [40–42].

B. α-cluster structure

In recent several decades, various theoretical models were developed to study the α-cluster structure, such as the Fermion molecular dynamics (FMD) model [60,61], the antisymmetric molecular dynamics (AMD) model [62,63], the extended quantum molecular dynamics (EQMD) model [26,64–66], and so on. In our simulation, the initial nucleon distribution in nuclei is configured in the HIJING model with either a pattern of Woods-Saxon distribution or an exotic nucleon distribution which is embedded to study the α-clustered structure [26,30]. The parameters set for the triangle structure are inherited from an EQMD model [26]. EQMD is extended from the QMD model, which can give reasonable α-cluster configurations for 4N nuclei by taking the effective Pauli potential and dynamical wave packet into account. More details for parameter setting can be seen in Refs. [26,30].

C. High momentum component (HMT)

The high-momentum-tail caused by short range correlation is also proposed to contribute to the longitudinal asymmetry in heavy-ion collisions. By comparing calculated results from the model with inclusive and exclusive experiments [37,38,67,68], the momentum distribution can be described as two parts: $n_0(k)$ corresponding to low-momentum part which is dominated by single particle features of nucleon structure, $n_1(k)$ corresponding to high-momentum part which is dominated by short-range properties of nucleon structure. In a simple way, one can write the momentum distribution as [68]

$$
\begin{cases}
n(k) \cong n_0(k) = \dfrac{1}{4\pi A} \displaystyle\sum_{\alpha < \alpha_F} A_\alpha n_\alpha(k) \text{ for } k < \hat{k} \\[2mm]
n(k) \cong n_1(k) = C^A n_{\text{deut}}(k) \text{ for } k > \hat{k}
\end{cases}, \quad (1)
$$

where the subscript F in α_F means Fermi level and Fermi momentum, and other variables can all be parametrized from light nuclei momentum distribution fitting [68]. For the above distribution, it is always compared with free-Fermi gas (FFG) distribution in this work. More details for parametrization can be found in Ref. [68]. In this work, we add this distribution into the initialization of AMPT model. The default case is the Woods-Saxon distribution, which generally describes only the potential of the nucleon. The FFG case is where the momentum distribution of all nucleons is below the Fermi momentum. However, for our focus—HMT—the nucleon's momentum could reach a high momentum tail, corresponding to $n_1(k)$ resulting from SRC.

D. Methodology

Generally, the longitudinal asymmetry can be characterized by some parameters [15]. Here, we give the rapidity shift y_0, asymmetry of participants α_{part}, and asymmetry of spectator α_{spec}:

$$
y_0 = \frac{1}{2} \ln \frac{A}{B}, \quad (2)
$$

$$
\alpha_{\text{part}} = \frac{A - B}{A + B}, \quad (3)
$$

$$
\alpha_{\text{spec}} = \frac{(N - A) - (N - B)}{(N - A) + (N - B)} = \frac{B - A}{2N - (A + B)}, \quad (4)
$$

where A and B are numbers of nucleons participating from the two colliding nuclei (naturally for identical nuclei A and B are equivalent), and N is the total number of nucleons in each nucleus. And it should be noted that $y_0 \cong \frac{1}{2} \ln \frac{A}{B}$ is appropriate when $m_0 \ll p$, fortunately it is possible in the LHC at TeV scale $m_0/p < 10^{-6}$ and in RHIC at GeV scale $m_0/p < 10^{-4}$. Hence we can also write the equation as $y_0 = \frac{1}{2} \ln \frac{1+\alpha_{\text{part}}}{1-\alpha_{\text{part}}}$. Further, when α_{part} is small enough, it is easy to see that $y_0 \approx \alpha_{\text{part}}$.

With these definitions we can classify vast events in terms of their y_0, for each event of a nucleus-nucleus collision has its own rapidity shift y_0 which is only determined by initial A and B. And although we cannot directly acquire the A and B, the practical experiments provide us an indirect method: by gaining energy deposited in the zero-degree calorimeters on either side of the interaction vertex in collider experiments [69], we can measure the α_{spec}, then y_0 can be calculated through the transformed equation

$$
y_0 = \frac{1}{2} ln \frac{(A + B)(1 + \alpha_{\text{spec}}) - 2N\alpha_{\text{spec}}}{(A + B)(1 - \alpha_{\text{spec}}) + 2N\alpha_{\text{spec}}}. \quad (5)
$$

And further, to keep consistent to the measurement α_{ZN} in ALICE experiments [69], the longitudinal asymmetry can also be defined by the number of neutrons in spectators, denoted as A_{spec}^n and B_{spec}^n, instead of α_{spec}:

$$
\alpha_{ZN} = \frac{A_{\text{spec}}^n - B_{\text{spec}}^n}{A_{\text{spec}}^n + B_{\text{spec}}^n}. \quad (6)
$$

In Fig. 1, according to different α_{ZN} regions [69], we plot y_0 distribution in Au + Au (Woods-Saxon case and HMT cases), C + C (Woods-Saxon, FFG, and HMT cases) collisions at center of mass energy $\sqrt{s_{NN}} = 200$ GeV, and C + C [Woods-Saxon and triangle (Tri.) case] at $\sqrt{s_{NN}} = 6.37$ TeV by using AMPT (string melting) model and the distribution is consistent with other models' simulations at RHIC or LHC energy [15,16,69].

In the distribution of y_0 shown in Fig. 1, we should note that if the nucleon intrinsic momentum distribution in the nuclei is taken into account, the definition of rapidity shift y_0 should be corrected as

$$
y_0 = \frac{1}{2} \ln \frac{1 + \alpha_{\text{mom}}}{1 - \alpha_{\text{mom}}}, \quad (7)
$$

where $\alpha_{\text{mom}} = \frac{|P_z^A| - |P_z^B|}{|P_z^A| + |P_z^B|}$, P_z^A and P_z^B are the longitudinal momentum of the participants from the two colliding nuclei. Note that P_z^A and P_z^B would be not equal to the beam momentum due to the effect of the nucleon intrinsic momentum distribution. Also for the FFG and HMT cases, the α_{ZN} which is used to divide positive or negative regions should take momentum distribution into account, the A_{spec}^n and B_{spec}^n in Eq. (6) should be naturally replaced by $P_z^{A_{\text{spec}}}$ and $P_z^{B_{\text{spec}}}$.

Now that we have the y_0 distribution classified by α_{ZN}, the longitudinal asymmetry of the different regions becomes obvious. Naturally, for events in $\alpha_{ZN} < -0.1$ region (which we call the negative α_{ZN} region), y_0 distribution shows us
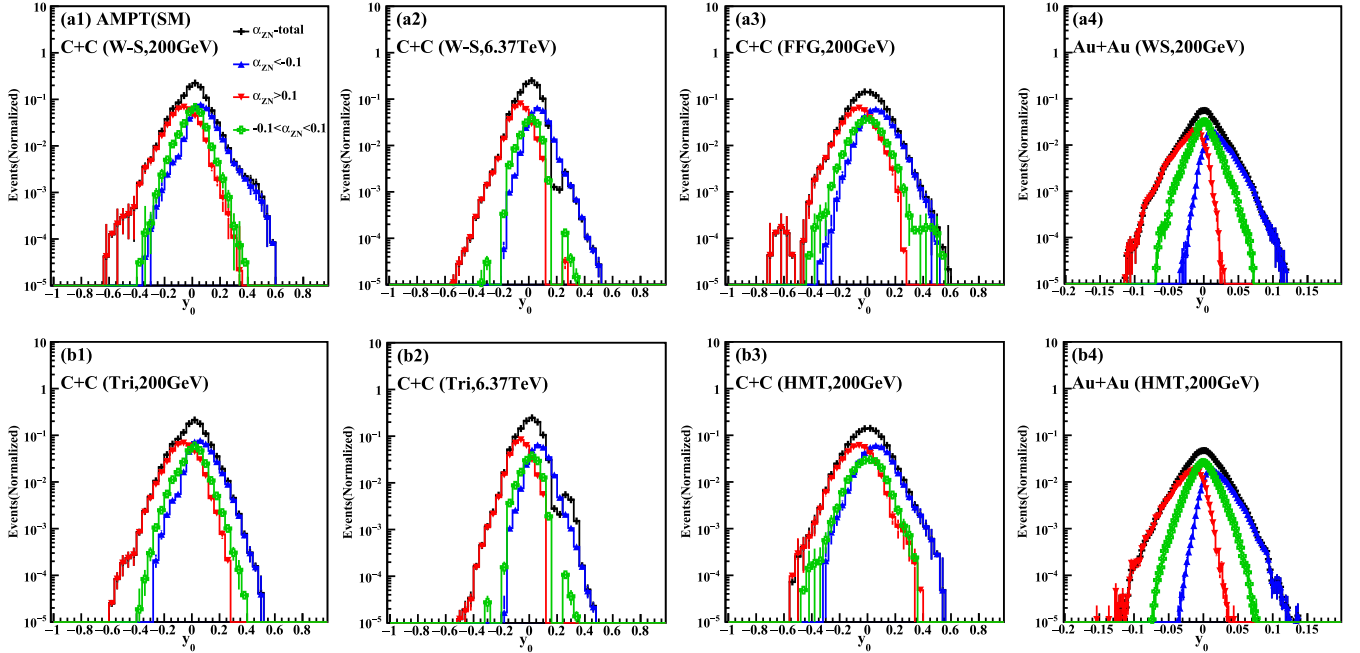
FIG. 1. Distribution of parameter y_0 in different α_{ZN} region for C + C at 200 GeV, C + C at 6.37 TeV, and Au + Au at 200 GeV with 0–10 % centrality in AMPT (string melting) frame.

a positive shift, also y_0 distribution for events in $\alpha_{ZN} > 0.1$ region (which we call positive α_{ZN} region) shows us a negative shift, and in the $|\alpha_{ZN}| < 0.1$ region, y_0 distributed in middle region. This negative correlation between α_{ZN} and y_0 can be understood from Eq. (4), for the behavior of y_0 intuitively reveals the physical picture of longitudinal asymmetry. For example, in an event, if $A > B$, we have $y_0 > 0$ according to Eq. (2). So the rest neutrons as spectators in the projectile (noted as A_{spec}^n) will generally be less than the rest neutrons as spectators in the target (noted as B_{spec}^n), thus we have $\alpha_{ZN} < 0$ according to Eq. (6).

Similarity between our y_0 distribution (especially in the Au+Au case) and the tuned Glauber Monte Carlo (TGMC) simulation of the Pb+Pb case by the ALICE Collaboration can be seen in Ref. [69]. And further we can see the charged particles' rapidity distribution of our eight systems in Fig. 2. It seems that our results are close to the ideal Gaussian distribution as proposed in Ref. [15] just by comparing our figures with works in Ref. [15] at RHIC energy. Then more issues beyond ideal cases or experimental results will also be discussed in this work, by fitting and the extraction of c_n we will see, besides the ideal Gaussian shape, the deformation of the rapidity shift will also reflect the longitudinal asymmetry, and fortunately we will disclose that the intrinsic momentum distribution can indeed affect the longitudinal asymmetry by changing the shape of rapidity distribution.

To further investigate the rapidity shift from the longitudinal asymmetry, it is proposed to take the ratio of the rapidity distribution of particles with positive asymmetry to that of negative asymmetry in collisions, $\frac{(\frac{dN}{dy})_{+asym}}{(\frac{dN}{dy})_{-asym}}$ [16], in which the '+asym' corresponds to positive y_0 region ($\alpha_{ZN} < -0.1$) and '−asym' corresponds to negative y_0 region ($\alpha_{ZN} > 0.1$), so

the ratio can be expressed in Taylor expansion,

$$\frac{\left(\frac{dN}{dy}\right)_{+asym}}{\left(\frac{dN}{dy}\right)_{-asym}} \propto \sum_0^\infty c_n y^n. \tag{8}$$

If the rapidity distribution of the particles is in a Gaussian type, $dN/dy \propto \exp(-\frac{(y-y_0)^2}{2\sigma^2})$, Eq. (8) becomes

$$\frac{\left(\frac{dN}{dy}\right)_{+asym}}{\left(\frac{dN}{dy}\right)_{-asym}} \propto \exp\left(\frac{2yy_0}{\sigma^2}\right) \propto \sum_0^\infty c_n(y_0, \sigma)y^n, \tag{9}$$

where the Taylor expansion coefficients c_n are related to the Gaussian parameters y_0 and σ and yield $c_n(y_0, \sigma) = \frac{(2y_0/\sigma^2)^n}{n!}$. However, the rapidity distribution of particles does not always follow a Gaussian pattern and the non-Gaussian effect will be discussed later.

III. RESULTS OF LONGITUDINAL ASYMMETRY FROM DIFFERENT SYSTEMS

A. y_0 and numbers of participants

Panels (a1)–(a4), (b1)–(b4) in Fig. 1 show the y_0 distributions at initial sate in C + C and Au + Au collisions at $\sqrt{s_{NN}} = 200$ GeV and C + C collisions at $\sqrt{s_{NN}} = 6.37$ TeV, respectively, for different α_{ZN} regions. The results are consistent with results for Au + Au simulation at RHIC energy and Pb + Pb measurement in ALICE experiment from various works [15,16,69]. In this calculation nucleon distributions are configured either as the Woods-Saxon type in ^{12}C or the α-clustered triangle shape in ^{12}C. The y_0 distributions in C + C collisions present similar behavior for the different configurations of the nucleon distribution in the collided nuclei, but show stronger fluctuations than for the larger collision
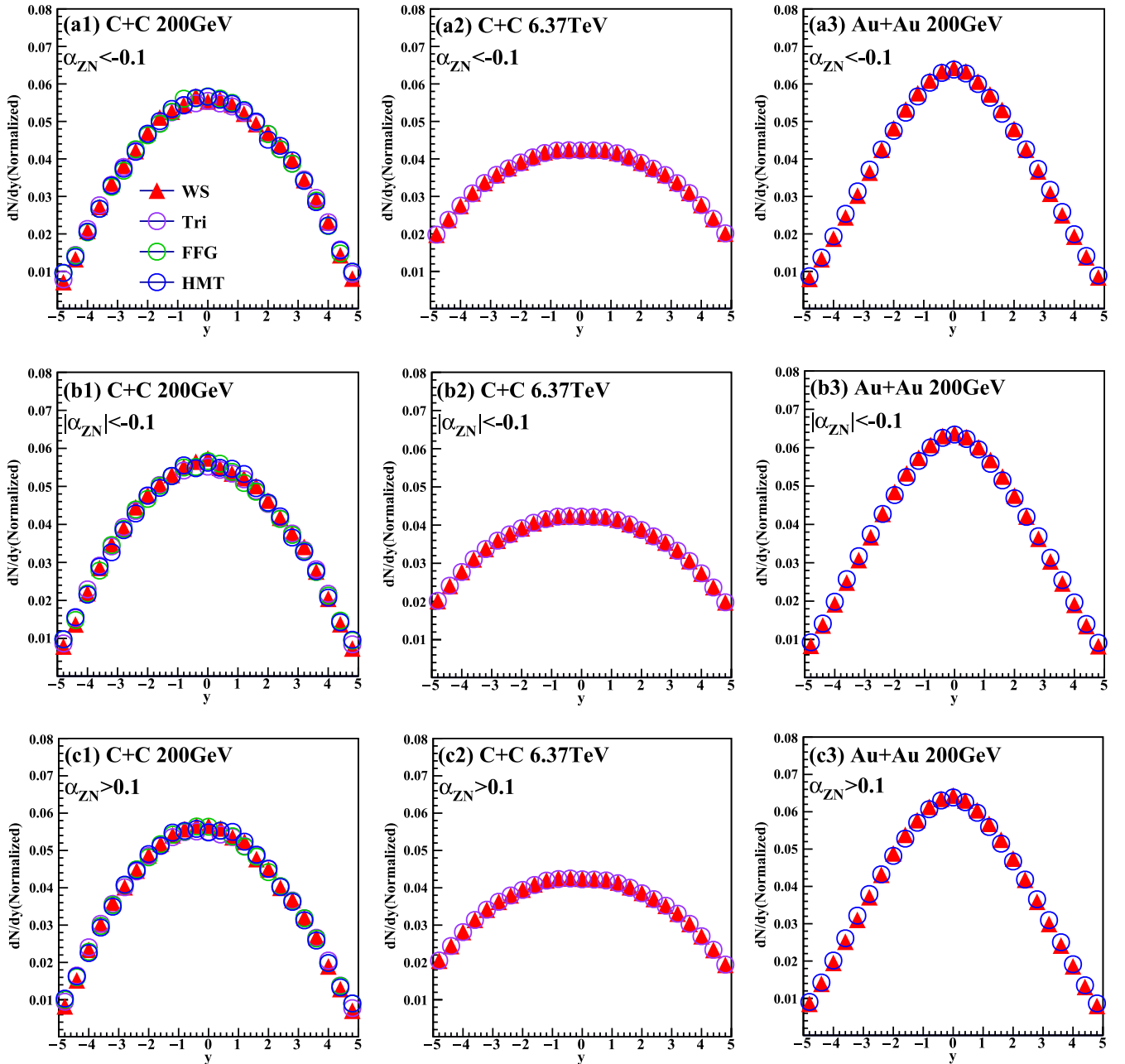
FIG. 2. Normalized dN/dy distribution in the positive, middle, negative y_0 regions for our eight different systems, corresponding to $\alpha_{ZN} < -0.1$, $-0.1 < \alpha_{ZN} < 0.1$, and $\alpha_{ZN} > 0.1$.

systems shown in Fig. 1(a4) and 1(b4), and also show stronger fluctuations than for larger $\sqrt{s_{NN}}$ in Fig. 1(a2) and 1(b2). For y_0 distributions in C + C collisions with configuration for collided nuclei with nucleon momentum distribution in HMT and FFG, it can be seen that the y_0 distribution in Fig. 1(a3) and 1(b3) is affected by the nucleon intrinsic momentum distribution comparing with that in Woods-Saxon distribution in Fig. 1(a1). The former case shows a larger width of the y_0 distribution contributed by momentum distribution.

Further in Fig. 1, by comparing C + C (WS, 200 GeV) to C + C (WS, 6.37 TeV), or C + C (Tri., 200 GeV) to C + C

(Tri., 6.37 TeV), the systems at higher $\sqrt{s_{NN}}$ (6.37 TeV) show smaller y_0 fluctuation than those at lower $\sqrt{s_{NN}}$ (200 GeV). And a large system (Au + Au) also shows smaller y_0 fluctuation than a small system (C + C). These physical pictures are consistent with works at RHIC energy in Ref. [15]. But if we consider initial intrinsic momentum distribution, we can see that y_0 fluctuation is enhanced by the unfixed momentum in beam direction (in FFG and HMT). Then in Fig. 2, it can be seen that the rapidity distribution at final state directly corresponds to different y_0 shift in Fig. 1. The rapidity distribution with positive shift in $\alpha_{ZN} < -0.1$ reflects the positive y_0 shift in $\alpha_{ZN} < -0.1$ and vice versa.
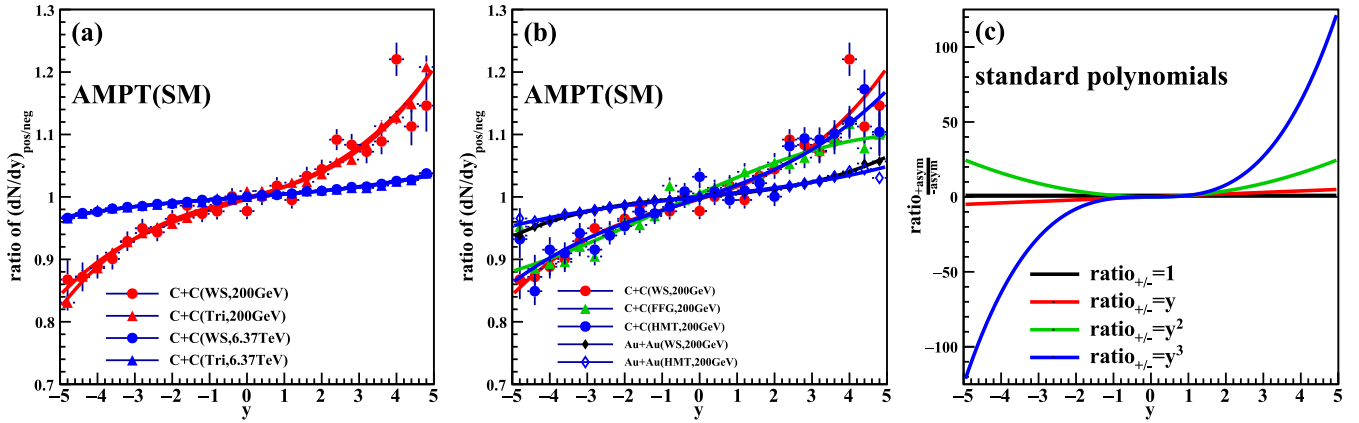
FIG. 3. The ratio of dN/dy for our eight different systems, along with fitting curves and standard polynomials for comparison.

B. Expansion coefficient

After plotting initial distribution of parameters, we can calculate c_n based on Eq. (8). It is clear that the longitudinal asymmetry becomes harder to be measured as the collision energy increases or the regions become close to the middle region [15], thus the later extraction of more parameters like expansion coefficients may become harder to distinguish in investigation. As a result, we choose taking positive and negative regions which are far from the midregion so that the events from both sides around symmetry events can provide distinct ratios to investigate further significant properties of longitudinal asymmetry.

The rapidity distributions of charged particles are shown in Fig. 2 for events from the positive and negative rapidity shift regions in C + C collisions and Au + Au collisions, respectively, for different initial state configurations and collision energies. To illustrate the longitudinal asymmetry, the differences between the positive and negative shift regions are expressed by the ratio of $\frac{(\frac{dN}{dy})_{+\text{asym}}}{(\frac{dN}{dy})_{-\text{asym}}}$ as shown in Fig. 3. According to Eqs. (8) and (9), a third order polynomial is performed to fit the ratio and the coefficients c_0, c_1, c_2, and c_3 are extracted [15,16]. The extracted coefficients c_n ($n = 0$, 1, 2, 3) are plotted in Fig. 4 for different collision systems with specific initial configurations.

For the α cluster structure case and the Woods-Saxon case in Fig. 4, at the same $\sqrt{s_{NN}}$, there is no obvious difference between c_n(Tri.) and c_n(WS) (here. $n = 1, 2, 3$) within the uncertainty for the same order. If we compare their central values, c_1 in the triangle case is slightly smaller than c_1 in the Woods-Saxon case, and c_2 behaves similarly to c_1, while c_3 is larger in the triangle case. In summary, the difference between the Woods-Saxon configuration and the cluster configuration is not clear.

For the case of intrinsic momentum distribution, according to Fig. 4, in C + C cases we can see that the first order terms c_1 in the WS case are smaller than those in the FFG and HMT cases. However, c_2 and c_3 in the WS case are larger than those in the FFG and HMT cases, respectively, and the high-order terms c_2, c_3 in the HMT case are larger than those in the FFG case, even considering their uncertainties. And it is interesting to see that the difference for c_n between Au+Au(WS)

and Au+Au(HMT) behaves similarly to the C+C system, suggesting to us that HMT may have a similar effect on longitudinal asymmetry in both small and large system sizes.

IV. EXPLANATION AND FURTHER DISCUSSION

A. Ideal Gaussian rapidity distribution and deformed rapidity distribution

Before discussing the results for c_n, we should first consider the parameters in ideal Gaussian distribution affect c_n. According to Eq. (9), c_n can be directly determined by initial shift y_0 and final rapidity width σ. However, in experiments or transport model simulations, the rapidity distribution does not always have the ideal Gaussian distribution, so that Eq. (9) requires $y_0^{+\text{asym}} = y_0^{-\text{asym}}$, $\sigma^{+\text{asym}} = \sigma^{-\text{asym}}$, which means that c_n is very sensitive to y_0, σ as explained in Ref. [69]. We can provide a simple method of estimating the magnitude of the sensitivity. We denote $\frac{\sigma^{+\text{asym}}}{\sigma^{-\text{asym}}} = m$, $\frac{y_0^{+\text{asym}}}{y_0^{-\text{asym}}} = n$, and choose $\sigma^{+\text{asym}} = \sigma$, $y_0^{+\text{asym}} = y_0$ (just for convenience), the widths and means in Fig. 2 give $(m - 1) \sim 10^{-3}$, $n \sim 10^{-1}$. Ignoring small higher order quantities such as $(1 - m^2)$, y_0^2, we can estimate the difference between the simulated rapidity distribution and the standard Gaussian shape: $\frac{ratio_{simu}}{ratio_{gaus}} \sim \exp \frac{m(n+1)yy_0}{\sigma^2}$. Both our simulation and Refs. [15,69] give $y_0 \sim 10^{-1}$, $\sigma \in (2, 4)$, so we can easily estimate that changing y_0 and σ in the order of 10^{-3}–10^{-1} can only lead to $ratio_{simu}$ being about 1.2 times larger than $ratio_{gaus}$. So, besides the sensitivity of y_0 and σ, we think that more of the difference of c_n is due to the deformation of the rapidity distribution.

Since c_n from different initial momentum cases show the most significant difference, we also choose to plot $Q - Q$ to compare our WS, FFG, and HMT cases with Gaussian distributions. In statistics, $Q - Q$ plots are usually used to characterize the normality of a given distribution, each distribution has its variable values corresponding to different percentiles, by plotting the scatter of our data sets on the y axis against the scatter of the Gaussian distribution on the x axis, we can visually see how close our data sets are distributed to a Gaussian distribution. In general, an approximate linearity like our fitted lines in Fig. 5 means that the distribution of our data is close to a Gaussian shape. And meanwhile the intercept
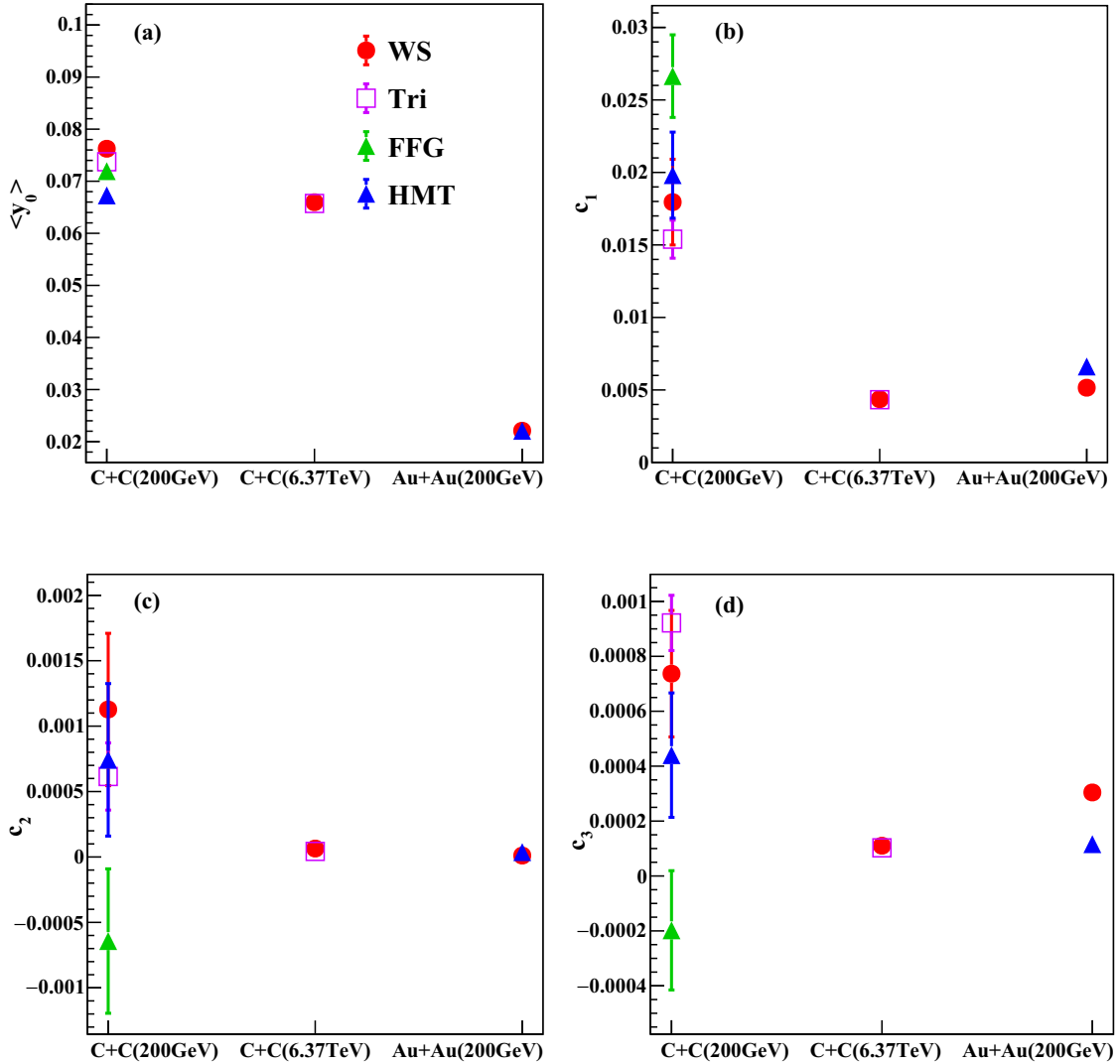
FIG. 4. $\langle y_0 \rangle$ and c_n extracted from our eight different systems, markers correspond to different configurations.

shows y_0 and the slope shows σ. The scatter and fitted lines in Fig. 5 do not show any significant difference between the WS, FFG, HMT cases and the Gaussian distribution. But we can still notice that the rapidity distribution with momentum distribution (FFG and HMT) give different slope and intercept from the WS case, implying to us the effect of intrinsic momentum distribution on rapidity deformation.

B. Effect on c_n from rapidity shift and rapidity deformation in longitudinal asymmetry

Beyond the explanation for the analytic form of the Gaussian distribution, the practical meaning of the expansion coefficient can be understood better from the definition of Taylor expansion that describes function by a combination of polynomials. From this point of view, our expansion coefficients c_n actually presents a contribution from powers of rapidity at different orders. To give a more intuitive explanation, we plot each rapidity ratio along with three standard polynomials: y, y^2, y^3 in Fig. 3(c). And then we also plot each component $c_n y^n$ in Fig. 6 to show their contribution to the ratio. Here, different values of c_n are shown in Fig. 4. It is

clear that in systems with higher $\sqrt{s_{NN}}$ (C + C, 6.37 TeV) or larger size (Au + Au, 200 GeV), the effect of longitudinal asymmetry is obviously smaller than that in C + C (200 GeV). In Fig. 6(a), 6(b), and 6(c), we can see yellow (C + C, WS, 6.37 TeV), green (C + C, Tri, 6.37 TeV), violet (Au + Au, WS, 200 GeV), and black (Au+Au, HMT, 200 GeV) lines are closer to 0 than red (C + C, WS, 200 GeV), orange (C + C, Tri, 200 GeV), cyan (C + C, FFG, 200 GeV), blue (C + C, HMT, 200 GeV) lines, and the longitudinal asymmetry of systems at the same $\sqrt{s_{NN}}$ with different configurations (C + C, WS, 200 GeV in red line and C + C, Tri, 200 GeV in orange line, C + C, WS, 6.37 TeV in yellow line, and C + C, Tri, 6.37 TeV in green line) are so close that they can hardly be distinguished. So our best choice to discuss how deformation changes the longitudinal asymmetry is to compare C + C (WS, 200 GeV), C + C (FFG, 200 GeV), and C + C (HMT, 200 GeV) systems.

In polynomials we can see, in different regions of rapidity, that the contribution of y, y^2, y^3 are different. As the rapidity y increases from 0 to 1, then to the region greater than 1, the deformation effect contributed by y^2 and y^3 becomes more
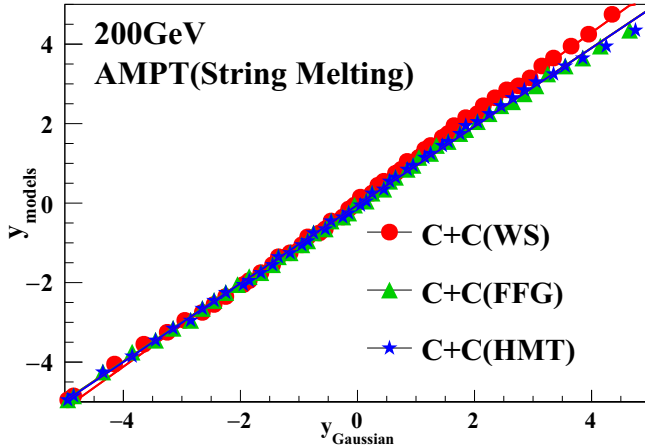
FIG. 5. The $Q - Q$ plot to examine normality of systems with different initial momentum and parametrize deformation effect at final rapidity distribution.

and more significant so that $c_n y^n$, especially $c_3 y^3$, can be comparable to $c_1 y^1$ as shown in Fig. 6(a),(c). In the $-1 < y < 1$ region, we have $|y| > |y^2| > |y^3|$, which means the direct rapidity shift y as the linear (also as the leading order) component of the ratio dominates the largest contribution to the ratio$_{+/-}$ in this region. According to Ref. [69], c_1 shows a linear dependence on $\langle y_0 \rangle$. For those cases in which y_0 only depends on the fluctuation of participants (like all the WS and Tri. cases), c_1 dependence on $\langle y_0 \rangle$ is consistent with our expectation and those simulation in ALICE. For systems at the same $\sqrt{s_{NN}}$ in the Woods-Saxon and Triangle cases, by comparing $\langle y_0 \rangle$ with c_1 in Fig. 4, we can see that c_1 shows similar linear dependence on $\langle y_0 \rangle$, and similar dependence can also be shown even in the error (width) of $\langle y_0 \rangle$ and c_1 in Fig. 4. We can see these c_1 in $|y| \in (0, 1)$ are mainly dominated by rapidity shift.

However, when we discuss the region in $y \in (1, 5)$, Fig. 6 reminds us that deformation of rapidity distribution also contributes to the ratio, meanwhile for the C+C FFG and HMT cases, their c_1 dependence on $\langle y_0 \rangle$ are different from the WS case. In Fig. 4 we can see FFG (200 GeV) and HMT (200 GeV) have smaller $\langle y_0 \rangle$ than WS (200 GeV), but larger c_1 than WS. In Fig. 2, it is difficult to see the slight deformation intuitively in the rapidity distribution. But fortunately, according to Figs. 1, 3, and 4, 6, we can infer how the rapidity distribution deformed at final state in Fig. 2.

For convenience, we can call the region in $|y - \langle y_0 \rangle| < \langle y_0 \rangle$ as peak, and the region in $2\langle y_0 \rangle < |y| < (5 - 2\langle y_0 \rangle)$ as ridge. In Fig. 3(b), we can see that around $y = 0$ both $C + C$ (FFG, 200 GeV, green) and $C + C$ (HMT, 200 GeV, blue) show larger ratios than $C + C$ (WS, 200 GeV, red). That means, in $|y| \in (0, 1)$ rapidity distribution in FFG and HMT give larger ratios of $\frac{(dN/dy)_{peak}}{(dN/dy)_{ridge}}$ than the WS case (normalized dN/dy has been shown in Fig. 2). This conclusion is a result from deformation of peak and ridge in Fig. 2, and in Fig. 1 we can infer the origin of this deformation.

In Fig. 1(a1), 1(a3), and 1(b3), we can extract that y_0 distribution in $C + C$ (FFG, 200 GeV) and $C + C$ (HMT, 200 GeV) show lower peaks and larger width than that in $C + C$ (WS,

200 GeV), namely, in $\alpha_{ZN} < -0.1$, $\sigma_{WS} = 0.1011 < \sigma_{FFG} = 0.1016 < \sigma_{HMT} = 0.1057$. These larger widths are caused by additional momentum distribution from FFG and HMT, as we defined in Eq. (7). Hence, we see the effect from intrinsic momentum distribution on longitudinal asymmetry at final state.

But momentum distribution does not only affect c_1 by causing deformation in $y \in (-1, 1)$. In Fig. 3(b), as y increases to ± 5, we can see that a ratio of $C + C$ (WS, 200 GeV, red) exceeds $C + C$ (FFG, 200 GeV, green) and $C + C$ (HMT, 200 GeV, blue), especially in $(-5, -4)$ and $(4, 5)$, after a small peak, the ratios in the FFG and HMT cases fall closer to 1.00 than the WS case. It reminds us that in the region close to ± 5, rapidity distributions in FFG and HMT are both depressed since obviously the ratios are closer to 1. This depression is a result of deformation at marginal y distribution ($y \to \pm 5$). To discuss the origin of this deformation, we should go back to check the asymmetry from the intrinsic momentum distribution in Fig. 1. By comparing initial y_0 distribution in Fig. 1 and final rapidity ratio in Fig. 3, we can see the asymmetry in both initial and final states is consistent. In y_0 distribution, FFG and HMT provide larger width around $y_0 = 0$ with less events around $y_0 = 0.6$ than the WS case. Meanwhile in Fig. 3, FFG and HMT show larger ratios in peak and ridge regions with smaller ratios in the marginal region. Comparison of c_n between WS, FFG, and HMT proved that asymmetry from FFG and HMT at initial state transformed into a different ratio at final state. Intrinsic momentum from FFG and HMT generates more events with larger y_0 in peak and ridge, corresponding to larger width of y_0, but the intrinsic momentum cannot support larger y_0 to extend to edge around $y_0 = 0.6$. Then the asymmetry transformed into rapidity asymmetry in Figs. 2 and 3, intrinsic momentum from FFG and HMT provides us enhanced ratio in peak and depressed ratio in ridge and margin. That is why we see larger c_1 and smaller c_2, c_3 in FFG and HMT than WS.

To test our interpretation, we also extract skewness and kurtosis of rapidity distribution in different systems and α_{ZN} regions in Fig. 7. According to knowledge from statistics, the skewness is defined as $\frac{\mu_3}{\sigma^3}$, and the kurtosis is defined as $\frac{\mu_4}{\sigma^4} - 3$, in which $\mu_n = \langle (X - \langle X \rangle)^n \rangle$ and $\sigma = \sqrt{\frac{\Sigma(X_i - \langle X \rangle)^2}{N}}$. The skewness describes how far the events distribution deviates from the mean value, for a standard Gaussian distribution the skewness is 0, and a positive skewness shows a longer small tail on the right of the mean value because a few events with higher X distribute on the right. And the kurtosis describes how the events concentrate around the mean value, for a standard Gaussian distribution the kurtosis is also 0, and higher kurtosis means more events distribute around the mean value. The values of skewness in four different configurations (WS, Tri, FFG, HMT) do not show significant dependence, but in the same configuration we can always see the skewness in the positive region is smaller than the one in the middle region. When both are smaller than the one in the negative region, the relationship is consistent to the physical picture of rapidity shift. The central values of kurtosis in FFG and HMT cases show a rising trend than Woods-Saxon cases as baseline. According to the statistical significance of kurtosis, higher kurtosis means more events concentrate to distribute around the mean value, that is to say, FFG and HMT cases
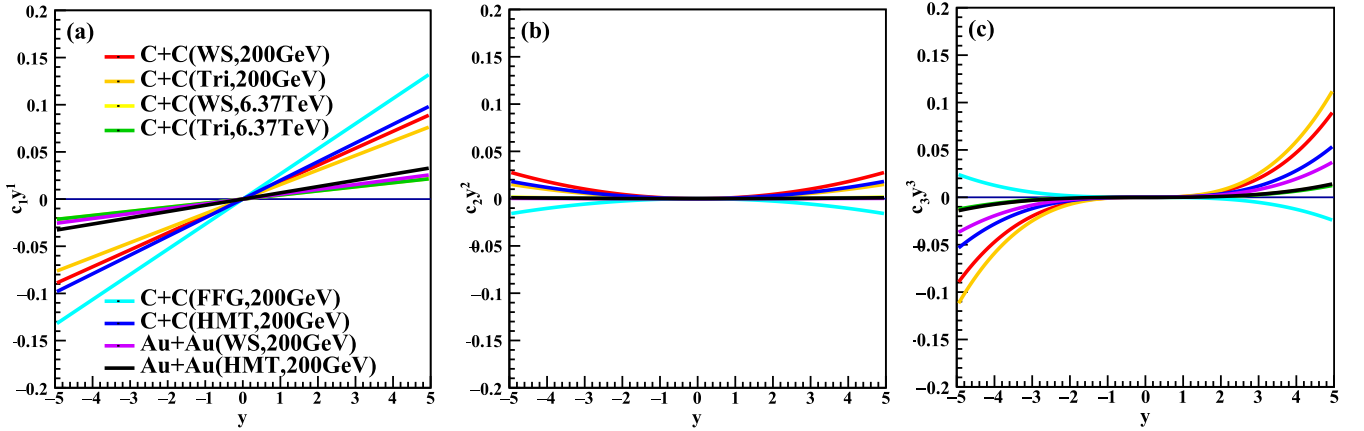
FIG. 6. Different components $c_n y^n$ for our eight systems.

have more events around the peak and less events in ridge and margin. This deformation of rapidity distribution leads to the anomaly of ratio and c_n. And further, comparing to the HMT case, larger kurtosis in the positive region and smaller kurtosis in the negative region in the FFG case means in the peak region more events distribute in +asym and less events distribute in −syem, which leads to higher c_1 in FFG than HMT. Here, we see that the kurtosis also supports our physical picture for the effect on longitudinal asymmetry from intrinsic momentum distribution.

Lastly, we can discuss the difference between FFG and HMT. According to Fig. 6, we can see that the fitting line of ratio$_{+/-}$ of FFG (green) is higher than HMT (blue) in most regions of peak and ridge as we mentioned in Fig. 2. Considering that c_1 dominates ratio$_{+/-}$ as shown in Fig. 6, we can say the effect of deformation in FFG is mainly shown as generating more events in the peak of rapidity distribution and less events at the edge close to ±5. It is reasonable that FFG indeed provides additional momentum distribution on y_0, because there is no interaction between nucleons, but meanwhile

FFG cannot provide more particles emitted to larger rapidity ($y \sim 5$). To compensate the over-increasing c_1 which dominates in the midrapidity region, c_2 and c_3 are both near enough to 0, even negative as shown in Figs. 6 and 4. But the SRC mechanism in HMT provides a way to emit more particles with larger rapidity. According to Refs. [37,38,67], HMT can cause more high energy nucleon emission at the final state, so in the beam direction more particles with larger rapidity can distribute close to ±5. That is why Figs. 4 and 6 show us that c_2, c_3 of HMT provide larger and positive contributions than those of FFG. In summary, intrinsic momentum distributions are transformed to different deformation of the final rapidity distribution, and their effect on longitudinal asymmetry can be characterized by c_n.

C. Prospect and alternative improvement in experiments

For both the initial condition and longitudinal asymmetry we introduced above, some experiments have been carried out to investigate them prospectively. Considering different
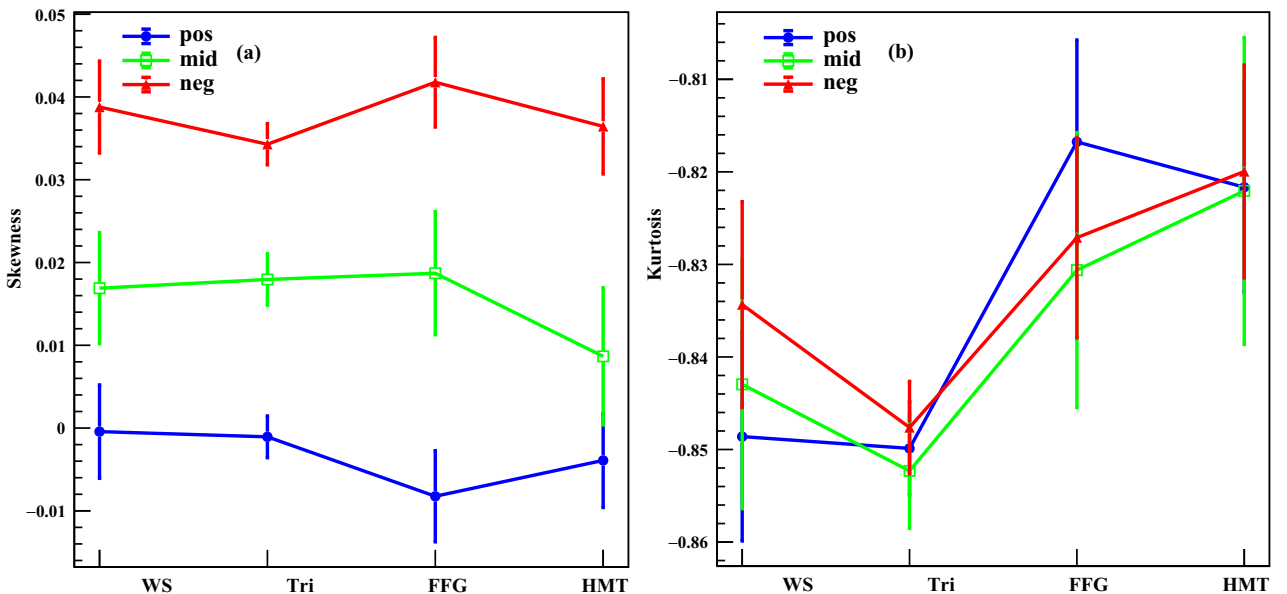
FIG. 7. The skewness and kurtosis of rapidity distribution from different configurations and α_{ZN} regions in our eight systems.

progresses in various experiments, here, we can simply show some feasibility on our suggested future experiments. The SRC experiments on Jefferson Laboratory extend to systems with larger removal energy, momentum, and more complex nuclei which can give us insights about effects from HMT. Measurements of rapidity distribution or longitudinal asymmetry in heavy ion collisions have been proceeded as Au+Au or Pb+Pb at RHIC and LHC. Also some are planned to investigate them at FRIB and FAIR, etc. [67,69]. It is possible to test some joint measurements, for instance, electron-nucleus scattering [70] experiments can help us estimate the HMT component and short-range-correlation effect in ion collisions [37,67], meanwhile collective flow v_n, characteristic spectra of giant dipole resonance (GDR), dihadron azimuthal correlation, and backward-forward multiplicity correlation can help us to distinguish α-cluster structure [26,30–33,35,71,72]. Lastly the energy deposition in the detector and rapidity measurement reveal the longitudinal asymmetry [69]. Also, for some practical application, we suggest to measure the rapidity spectrum or compare with previous data, and use probes of the α cluster or HMT mentioned above in RHIC or ALICE experiments to distinguish different configurations, then measure coefficients $\langle y_0 \rangle$ and c_n in different configurations to match their longitudinal asymmetry. Then according to our work one can give these systems' initial rapidity shift and nonzero momentum shift, which can be used to reconstruct the colliding vertex or correct the initial angular momentum, this reconstruction and correction may affect the initial condition in the polarization problem, chiral magnetic effect measurement, and so on, so we hope our work on longitudinal asymmetry can be applied in observable measurements in these experiments. Despite the limited progress of the experimental program, RHIC and ALICE have provided us abundant benchmarks for the rapidity distribution and longitudinal asymmetry of various systems. These results can benefit future measurements that may be performed in more experiments on different colliders and systems such as O+O colliding at FRIB, SRC experiments at JLab, and so on. By carrying out these experiments in symmetric nuclei collisions, we can give insight or provide an improvement of the physical picture on longitudinal asymmetry, further to constrain conditions of collision and describe final rapidity more precisely.

V. SUMMARY

This paper presents a comparison of the longitudinal asymmetry for systems with different α cluster structure and intrinsic momentum distribution in AMPT model. α_{ZN} and y_0 are calculated to characterizing the rapidity shift, as performed in experimental measurements by ALICE [69]. To study the effect of different initial conditions on longitudinal asymmetry, we introduce α cluster structure and different intrinsic nucleon momentum distribution into the simulation in AMPT

model, where the intrinsic momentum distribution is added to the parameter y_0 as shown in Fig. 1(a3) and 1(b3). With these data we use a third polynomial fitting to extract the expansion coefficients c_n in Fig. 4. The comparison among different initial conditions shows us the effects of the α clustering structure and the initial momentum component.

Based on our analysis, we propose that the dependence of the longitudinal asymmetry is the result of the competition between the rapidity shift and rapidity deformation. In the $|y| < 1$ region, c_1 is mainly linearly dependent on the initial rapidity shift if we do not consider the momentum distribution, and the momentum distribution will lead to rapidity deformation, shown as a larger ratio in peak and ridge. However, in the large rapidity region, c_2 and c_3 reflect the deformation of the final-state rapidity distribution. HMT caused by SRC provides a larger rapidity distribution when y is close to ± 5, which enhances the longitudinal asymmetry of c_2 and c_3. To further support our interpretation, we extracted the skewness and kurtosis from different configurations. By comparing skewness and kurtosis from different shift regions and configurations, we demonstrate that the particle rapidity distribution caused by different configurations, especially FFG and HMT, provide deformation in different regions as expected, resulting in additional longitudinal asymmetry. And this phenomenon shows a consistency with the anomaly of coefficients c_n, which can be measured in future experiments.

Finally, we discuss the practical application of our calculation in experiments, including a joint measurement on the α-clustering effect, high momentum component effect, and longitudinal asymmetry with deformation, some dependent experiments have been performed in different detectors [31,34,67,69]. And we respectively introduced different experiments for the joint measurement, so that researchers can ensure the feasibility of suggested experiments in the future. In order to test the results of this work, we propose to investigate the collision of symmetric nuclei of the C + C system, and in the future we expect that these investigations by observables related to initial conditions can provide us with insights to constrain the nuclear structure and the intrinsic momentum distribution of the nucleon in the nuclear, as well as the correction for the deformation of the final rapidity distribution.

[1] M. Connors, C. Nattrass, R. Reed, and S. Salur, Rev. Mod. Phys. **90**, 025005 (2018).

[2] A. Bzdak, S. Esumi, V. Koch, J. F. Liao, M. Stephanov, and N. Xu, Phys. Rep. **853**, 1 (2020).

[3] A. Rothkopf, Phys. Rep. **858**, 1 (2020).
[4] J. Chen, D. Keane, Y. G. Ma, A. Tang, and Z. Xu, Phys. Rep. **760**, 1 (2018).
[5] M. I. Abdulhamid *et al.*, Phys. Rev. Lett. **130**, 202301 (2023).
[6] A. Tumasyan *et al.*, Phys. Rev. Lett. **129**, 022001 (2022).
[7] L. L. Zhu, B. Wang, M. Wang, and H. Zheng, Nucl. Sci. Tech. **33**, 45 (2022).
[8] M. Wang, J. Q. Tao, H. Zheng, W. C. Zhang, L. L. Zhu, and A. Bonasera, Nucl. Sci. Tech. **33**, 37 (2022).
[9] S. W. Lan and S. S. Shi, Nucl. Sci. Tech. **33**, 21 (2022).
[10] Y. C. Liu and X. G. Huang, Sci. China Phys. Mech. Astron. **65**, 272011 (2022).
[11] Y. Zhang, D. Zhang, and X. Luo, Nucl. Tech. (in Chinese) **46**, 040001 (2023).
[12] C. M. Ko, Nucl. Sci. Tech. **34**, 80 (2023).
[13] K. Sun, L. Chen, C. M. Ko, F. Li, J. Xu, and Z. Xu, Nucl. Tech. (in Chinese) **46**, 040012 (2023).
[14] R. Rapp, Nucl. Sci. Tech. **34**, 63 (2023).
[15] S. Thakur, K. Saha Sumit *et al.*, Eur. Phys. J. A **58**, 13 (2022).
[16] R. Raniwala, S. Raniwala, and C. Loizides, Phys. Rev. C **97**, 024912 (2018).
[17] X.-G. Deng, X.-G. Huang, and Y.-G. Ma, Phys. Lett. B **835**, 137560 (2022).
[18] M. Bleicher, E. Zabrodin, C. Spieles *et al.*, J. Phys. G **25**, 1859 (1999).
[19] K. Xiao, P. C. Li, Y. J. Wang, F. H. Liu, and Q. F. Li, Nucl. Sci. Tech. **34**, 62 (2023).
[20] P. C. Li, J. Steinheimer, T. Reichert *et al.*, Sci. China Phys. Mech. Astron. **66**, 232011 (2023).
[21] B.-S. Xi, X.-G. Deng, S. Zhang, and Y.-G. Ma, Eur. Phys. J. A **59**, 33 (2023).
[22] F. Kornas (for HADES Collaboration), talk given at Strangeness Quark Matter 2021 Online.
[23] M. S. Abdallah *et al.* (STAR Collaboration), Phys. Rev. C **104**, L061901 (2021).
[24] G. Gamow and E. Rutherford, Proc. Math. Phys. Eng. Sci. **126**, 632 (1930).
[25] L. Qin, K. Hagel, R. Wada *et al.*, Phys. Rev. Lett. **108**, 172701 (2012).
[26] W. B. He, Y. G. Ma, X. G. Cao, X. Z. Cai, and G. Q. Zhang, Phys. Rev. Lett. **113**, 032506 (2014).
[27] W.-B. He, Q.-F. Li, Y.-G. Ma, Z.-M. Niu, J.-C. Pei, and Y.-X. Zhang, Sci. China Phys. Mech. Astron. **66**, 282001 (2023).
[28] W. He, Y. Ma, L. Pang, H. Song, and K. Zhou, Nucl. Sci. Tech. **34**, 88 (2023).
[29] W. Broniowski and E. Ruiz Arriola, Phys. Rev. Lett. **112**, 112501 (2014).
[30] Y.-A. Li, S. Zhang, and Y.-G. Ma, Phys. Rev. C **102**, 054907 (2020).
[31] C.-C. Guo, W.-B. He, and Y.-G. Ma, Chin. Phys. Lett. **34**, 092101 (2017).
[32] Y.-A. Li, D.-F. Wang, S. Zhang, and Y.-G. Ma, Chin. Phys. C **46**, 044101 (2022).
[33] Y.-A. Li, D.-F. Wang, S. Zhang, and Y.-G. Ma, Phys. Rev. C **104**, 044906 (2021).
[34] Y.-G. Ma and S. Zhang, Influence of nuclear structure in relativistic heavy-ion collisions, in *Handbook of Nuclear Physics*, edited by I. Tanihata, H. Toki, and T. Kajino (Springer Nature, Singapore, 2020), pp. 1–30.
[35] Y.-G. Ma, Nucl. Tech. (in Chinese) **46**, 080001 (2023).
[36] A. N. Antonov, V. A. Nikolaev, and I. Z. Petkov, Z. Phys. A **297**, 257 (1980).
[37] C. Ciofi degli Atti, S. Simula, L. L. Frankfurt, and M. I. Strikman, Phys. Rev. C **44**, R7(R) (1991).
[38] Z. Wang, C. Xu, Z. Ren, and C. Gao, Phys. Rev. C **96**, 054603 (2017).
[39] L. Shen, B.-S. Huang, and Y.-G. Ma, Phys. Rev. C **105**, 014603 (2022).
[40] Z.-W. Lin, C. M. Ko, B.-A. Li, B. Zhang, and S. Pal, Phys. Rev. C **72**, 064901 (2005).
[41] G.-L. Ma and Z.-W. Lin, Phys. Rev. C **93**, 054911 (2016).
[42] Z.-W. Lin and L. Zheng, Nucl. Sci. Tech. **32**, 113 (2021).
[43] X.-N. Wang and M. Gyulassy, Phys. Rev. D **44**, 3501 (1991).
[44] M. Gyulassy and X.-N. Wang, Comput. Phys. Commun. **83**, 307 (1994).
[45] B. Zhang, Comput. Phys. Commun. **109**, 193 (1998).
[46] B.-A. Li and C. M. Ko, Phys. Rev. C **52**, 2037 (1995).
[47] X.-H. Jin, J.-H. Chen, Y.-G. Ma *et al.*, Nucl. Sci. Tech. **29**, 54 (2018).
[48] H. Wang, J. H. Chen, Y. G. Ma *et al.*, Nucl. Sci. Tech. **30**, 185 (2019).
[49] H. Wang and J. H. Chen, Nucl. Sci. Tech. **33**, 15 (2022).
[50] Z.-W. Lin, Phys. Rev. C **90**, 014904 (2014).
[51] C. Shen and Y. Li, Nucl. Sci. Tech. **31**, 122 (2020).
[52] R.-X. Cao, S. Zhang, and Y.-G. Ma, Phys. Rev. C **106**, 014910 (2022).
[53] Q. Chen, G. Ma, and J. Chen, Nucl. Tech. (in Chinese) **46**, 040013 (2023).
[54] X.-L. Zhao, G.-L. Ma, and Y.-G. Ma, Phys. Rev. C **99**, 034903 (2019).
[55] J.-H. Gao, G.-L. Ma, S. Pu, and Q. Wang, Nucl. Sci. Tech. **31**, 90 (2020).
[56] Y.-C. Liu and X.-G. Huang, Nucl. Sci. Tech. **31**, 56 (2020).
[57] C.-Z. Wang, W.-Y. Wu, Q.-Y. Shou, G.-L. Ma, Y.-G. Ma, and S. Zhang, Phys. Lett. B **820**, 136580 (2021).
[58] X. L. Zhao, G. L. Ma, and Y. G. Ma, Phys. Lett. B **792**, 413 (2019).
[59] W.-Y. Wu, C.-Z. Wang, Q.-Y. Shou, Y.-G. Ma, and L. Zheng, Phys. Rev. C **103**, 034906 (2021).
[60] H. Feldmeier, Nucl. Phys. A **515**, 147 (1990).
[61] M. Chernykh, H. Feldmeier, T. Neff, P. von Neumann-Cosel, and A. Richter, Phys. Rev. Lett. **98**, 032501 (2007).
[62] Y. Kanada-En'yo, M. Kimura, and A. Ono, Prog. Theor. Exp. Phys. **2012**, 01A202 (2012).
[63] Y. Kanada-En'Yo, M. Kimura, and H. Horiuchi, Eur. Phys. J. A **25**, 305 (2005).
[64] W. B. He, Y. G. Ma, X. G. Cao, X. Z. Cai, and G. Q. Zhang, Phys. Rev. C **94**, 014301 (2016).
[65] B. S. Huang, Y. G. Ma, and W. B. He, Phys. Rev. C **95**, 034606 (2017).
[66] S. S. Wang, X. G. Cao, and T. L. Zhang, Nucl. Phys. Rev **32**, 24 (2015).
[67] M. Patsyuk *et al.*, Nat. Phys. **17**, 693 (2021).
[68] C. Ciofi degli Atti and S. Simula, Phys. Rev. C **53**, 1689 (1996).
[69] S. Acharya, J. Adam *et al.*, Phys. Lett. B **781**, 20 (2018).
[70] S. Li, R. Cruz-Torres, N. Santiesteban *et al.*, Nature (London) **609**, 41 (2022).
[71] C. Zhang, A. Behera, S. Bhatta, and J. Jia, Phys. Lett. B **822**, 136702 (2021).
[72] B. Alver and G. Roland, Phys. Rev. C **81**, 054905 (2010).